

Research Article

A Simplified Finite Control Set Model Predictive Control for T-Type Three-Level Power Conversion System Based on LCL Filter

Ning Gao , Huaiyu Fan, and Weimin Wu 

Department of Electrical Engineering, Shanghai Maritime University, Pudong District, Shanghai 201306, China

Correspondence should be addressed to Ning Gao; ngao@shmtu.edu.cn

Received 3 March 2021; Accepted 13 May 2021; Published 1 June 2021

Academic Editor: Carlos-Andrés García

Copyright © 2021 Ning Gao et al. This is an open access article distributed under the Creative Commons Attribution License, which permits unrestricted use, distribution, and reproduction in any medium, provided the original work is properly cited.

Finite control set model predictive control (FCSMPC) is a highly attractive and potential control method for grid-tied converters. However, there are several challenges when employing FCSMPC in an LCL filter-based T-type three-level power conversion system (PCS) for battery energy storage applications. These challenges mainly include the increasing complexity of control algorithm and excessive cost of additional sensors, which deteriorate the performance of PCS and limit the application of FCSMPC. In order to overcome these issues, this paper proposes a simplified FCSMPC algorithm to reduce the computation complexity. Furthermore, full-dimensional state observers are adopted and implemented to estimate the instantaneous values of grid-side current and capacitor voltage for purpose of removing unnecessary electrical sensors. The implementation of proposed FCSMPC algorithm is described step by step in detail. Simulation results are provided as a verification for the correctness of theoretical analysis. Finally, a three-phase T-type three-level PCS prototype rated at 2.30 kVA/110 V is built up. Experimental results extracted from the prototype can verify the effectiveness of the proposed control strategy.

1. Introduction

Sustainable energy sources widely utilized in the power system leads to instability issues due to their undispachable generating features [1, 2]. For this reason, the demand for energy storage system is growing remarkably for decades [3–5]. Battery energy storage system (BESS), highlighted by its fast response, economic acceptable, long cycle life, high density, and low installation requirement, is believed to be one of the best choices to provide a series of reliable electricity services among various kinds of energy storage techniques [6].

PCS plays an important role as a specific bidirectional AC-DC converter in the BESS to interface battery units with the grid based on power electronics semiconductor techniques [7]. Three-phase two-level voltage source converter (2L-VSC) is commonly used in grid-tied converter applied in photovoltaic generation or wind turbines. However, its drawbacks, mainly including high voltage stress and poor harmonic performance, limit the further development of 2L-VSC especially in large-scale energy storage scenario.

Three-level voltage source converter (3L-VSC) topologies are much more advantageous than 2L-VSC in this application for its beneficitions of lower output harmonics, higher efficiency, more compact structure, and reduced voltage changing rate [8]. A lot of 3L-VSC topologies have been reported and studied recently, such as neutral-point-clamped VSC [9], active NPC VSC [10], cascaded H-bridge topology [11], flying capacitor VSC [12], and T-type 3L-VSC [13]. T-type 3L-VSC is now receiving high priority to the development because six clamped diodes are removed compared to traditional NPC. On the other hand, T-type 3L-VSC owns less conduction loss, which means it is able to promote the efficiency if switching frequency is below 30 kHz [13]. Aside from the active components in the PCS, passive filter based on LCL structure tends to be adopted since it provides superior performance in high-order harmonics attenuation [14].

It is significant to select a convenient control strategy for the PCS to obtain high-quality current injected to the grid. Various kinds of linear and nonlinear control methods are all verified choices to solve the control problem. Model

predictive control (MPC) is an attractive model-based nonlinear optimal control strategy widely used in industrial areas [15, 16]. MPC applied in power electronics control area can be roughly divided into two categories: one is continuous control set MPC and the other is finite control set MPC. By comparing these two methods, FCSMPC uses the discrete nature of PCS which means the number of available switching states is finite. By evaluating them in terms of cost function and control restrictions, the most suitable switching state will be determined to be active later. As reported in [17], high performance of FCSMPC algorithm which is successfully implemented in an LCL-based grid-tied 2L-VSC has been confirmed by both simulation and experimental investigations.

Although FCSMPC can also be adopted in a 3L-VSC, further improvement and extra strategy need to be studied because of the increased complexity of 3L-VSC and DC-link voltage balancing problem [18]. In practice, the calculation time of control algorithm will unavoidably become longer because repeating times for transferring predictive model and calculating cost function increase apparently along with the number of switching states, which is equal to 27 for 3L-VSC compared to 8 for 2L-VSC. In order to resolve this contradiction, researchers have proposed several methods to attenuate the computational burden of FCSMPC.

In [19], a simplified computational method was proposed by introducing the Lyapunov principle into the design of sector distribution method based on space vector modulation technique for a nested neutral-point-clamped converter. By using the proposed method, the unwanted switching states can be eliminated and only 9 vectors, rather than for all the 64 vectors, need to be evaluated in total. In [20], an effective approach with equivalent transformation and specialized sector distribution was presented to reduce the running time without affecting the control performance. The proposed method can be used in various circuit topologies with multiple constraints. In [21], a simplified algorithm based on a new direct torque control switching table was presented. Based on this method, only three voltage vectors instead of eight are used for prediction and actuation. Moreover, the number of prediction vectors is reduced without any complex calculations.

Removing the nonessential sensors is also an important topic to compare hardware cost and further exploit the merits of FCSMPC. In [22], a model calculation method with inverter voltage and current was proposed to estimate the capacitor voltage and grid current by ignoring the capacitor current. However, the assumption of ignoring capacitor current is only valid for the case that the impedance of the capacitor branch is much higher than the inductor branch. In [23], an effective method was presented to decrease the sensors of state variables. In the proposed method, the capacitor current loop was merged with the grid-injected current loop by transforming the block diagram; thus a kind of capacitor current sensor could be saved. Furthermore, full-order state observer [24] and Kalman filter [25] based on state-space model were investigated, which were both utilized to estimate the state variables of filter via the closed-loop system.

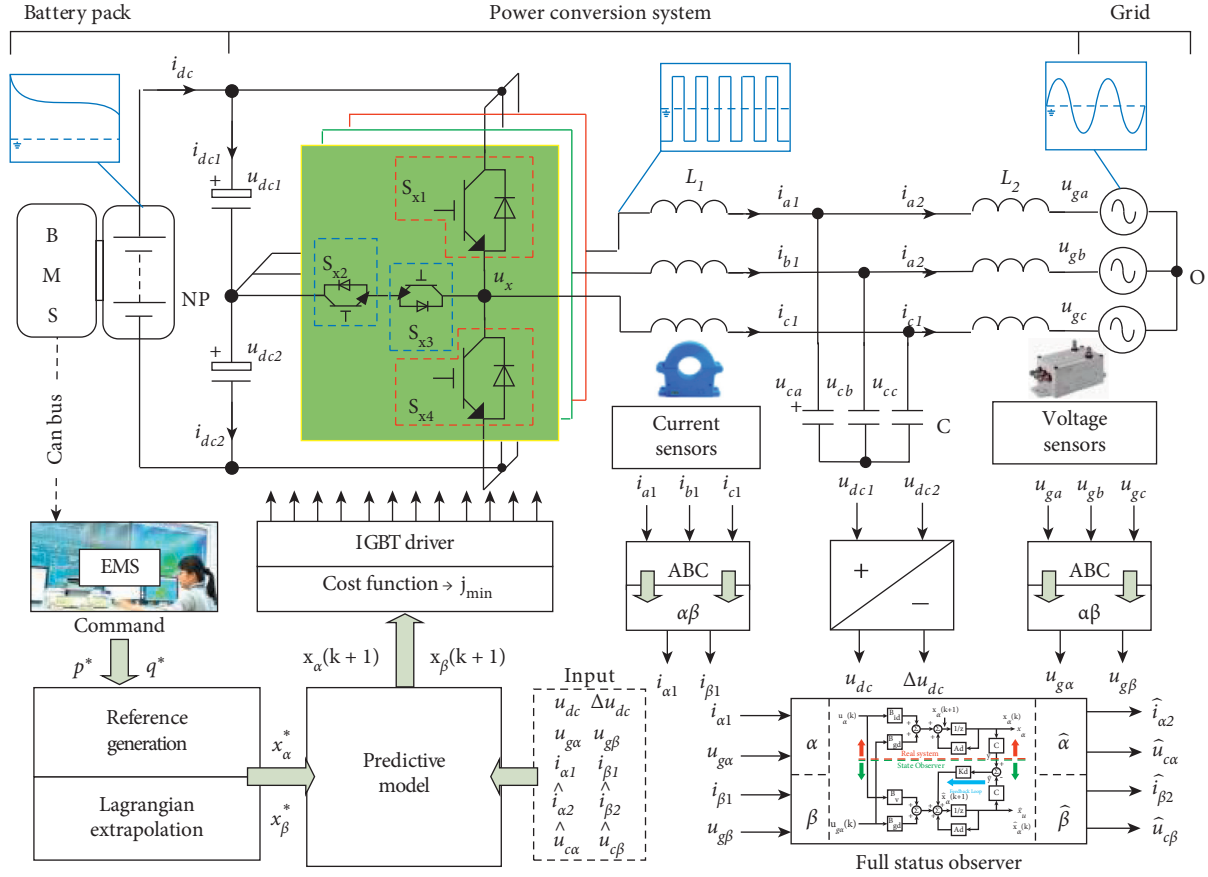
Therefore, this paper proposes a simplified FCSMPC for a three-phase PCS based on T-type three-level topology to reduce its computational burden. Compared with the MPC strategy in [17], full-dimensional state observers are adopted for estimating the grid-side current and capacitor voltage within LCL filter for purpose of saving the unnecessary sensors. The remainder of this paper is organized as follows. Section 2 briefly introduces the system configuration and basic principle of FCSMPC. In Section 3, a detailed discrete predictive model of PCS is deduced. Based on this model, a description of the proposed simplified FCSMPC strategy is given from the view of reference generation, control set optimization, cost function, and state observers. Section 4 shows the simulation and experimental results for purpose of verifying the control algorithm in this paper. Finally, a brief conclusion is summarized in Section 5.

2. System Configuration and Description

Figure 1 shows the basic structure of PCS for BESS application. The battery pack which performs as the main electrochemical reaction-based energy storage component characterized by its high density and flexibility is coupled to the grid using PCS composed of a bidirectional three-phase T-type three-level AC-DC converter and LCL filter. Three-level power conversion topologies usually exhibit outstanding performances including total harmonic distortion (THD) and efficiency compared to traditional two-level converter, while high-order passive filter is able to attenuate high frequency harmonics more effectively than a single L filter.

As general definitions of common variables, i_{a1} , i_{b1} , and i_{c1} represent the phase current flowing through inverter-side inductor L_{1a} , L_{1b} , L_{1c} . i_{a2} , i_{b2} , and i_{c2} are phase current flowing through grid-side inductor L_{2a} , L_{2b} , and L_{2c} . u_{ca} , u_{cb} , and u_{cc} represent the filtering capacitor voltages. u_a , u_b , and u_c represent the output voltage of each phase legs, respectively. u_{ga} , u_{gb} , and u_{gc} are grid voltages. Voltage and current sensors are installed properly for signal acquisition. u_{dc1} represents the voltage across the top-side capacitor, and u_{dc2} represents voltage of bottom-side capacitor. Moreover, when analysing the instantaneous power control of PCS, the battery pack can be assumed as a stiff DC voltage source because its output voltage u_{bat} varies slowly enough compared to the microsecond time-scale of PCS's real-time control in most cases. The PCS is supervised by the superior energy management system, which decides the output feature of BESS by sending the active power reference p^* and reactive power reference q^* instructions to the PCS.

Each phase leg of T-type 3L-VSC in the PCS depicted in Figure 1 consists of four semiconductor switches named as $S_{x1} \sim S_{x4}$ ($x = a, b, c$), which can be divided into two groups: two main switches S_{x1} and S_{x4} , and two auxiliary switches S_{x2} and S_{x3} . Among these switches, driver signal of S_{x1} is complementary to S_{x3} , and driver signal of S_{x2} is complementary to S_{x4} , respectively. There are three output states in every phase leg: (1) "P" state: if S_{x1} and S_{x2} turn on simultaneously, in the same time S_{x3} and S_{x4} turn off. The output voltage of phase leg is equal to $u_{bat}/2$ with reference to



Chemical En.

↔ DC En.

↔ Low-quality AC En.

↔ Standard AC En.

FIGURE 1: Structure of T-type three-level power conversion system for battery energy storage application.

the neutral point (NP) of the DC-link upon the assumption that NP is balanced in steady state which means $u_{dc1} = u_{dc2} = +u_{bat}/2$. (2) “0” state: if S_{x2} and S_{x3} turn on simultaneously, while S_{x1} and S_{x4} turn off in the same time, the midpoint of the phase leg connects to NP directly. The output voltage is zero in this state. (3) “N” state: if S_{x3} and S_{x4} turn on simultaneously, while S_{x1} and S_{x2} turn off in the same time. Similar to P state, the output voltage of phase leg is $-u_{bat}/2$.

Therefore, the PCS is able to generate totally 27 space vectors in stationary reference frame. The control set of PCS is defined to include all the combinations of switching states illustrated in Figure 2. It is also named as space vector distribution diagram, which aims to describe their magnitudes and positions. According to the lengths of voltage vectors, there are 6 large, 6 medium, 12 small, and three zero vectors possibly generated by the PCS. It can be seen that small vectors, for instance, vectors P00 and 0NN, exert an identical effect on the output current of PCS. Therefore, these pairs of small vectors can be used to balance the neutral point voltage which will be discussed later. The

detailed relations between space vector and switching status are depicted in Figure 3.

The FCSMPC algorithm is needless to involve a modulation stage like traditional control method such as proportional-integrator control widely applied in grid-tied converter. Modified FCSMPC scheme in this paper is carried out in the $\alpha\beta$ reference frame including six steps as follows:

- (1) Signal regulation and acquisition, using A/D converter of the digital processor to obtain the instantaneous value of i_{x1} , u_{gx} ($x = a, b, c$), u_{dc1} and u_{dc2} . Mind that unlike conventional FCSMPC method, u_{cx} and i_{x2} are not necessary to be sampled because observer technique is adopted afterwards.
- (2) Calculate the references in the next sampling period according to the external references p^* and q^* commanded by the upstream supervisor system.
- (3) Estimate u_{cx} and i_{x2} based on full-dimensional state observers.
- (4) Construct the prediction model. This is a two-step process. First, make the vector search span smaller

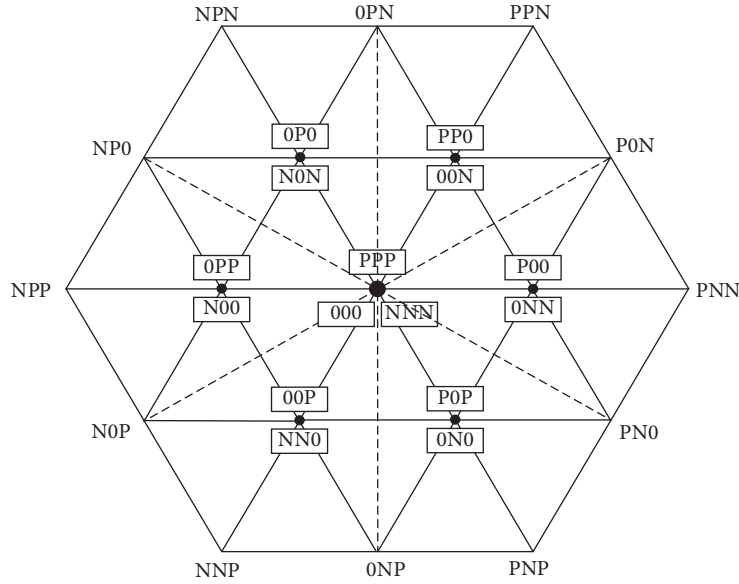


FIGURE 2: Distribution diagram of space vectors in $\alpha\beta$ reference frame.

Vector	1	PNN	2	PON	3	PPN	4	OPN	5	NPN	6	NPO	7	NPP	8	NOP	9	NNP
$[u_\alpha \ u_\beta]$		$[2u_d / 3 \ 0]$		$[u_d / 2 - \sqrt{3}u_d / 6]$		$[u_d / 3 - \sqrt{3}u_d / 3]$		$[0 \ \sqrt{3}u_d / 3]$		$[-u_d / 3 - \sqrt{3}u_d / 3]$		$[-u_d / 2 \ \sqrt{3}u_d / 6]$		$[-2u_d / 3 \ 0]$		$[-u_d / 2 - \sqrt{3}u_d / 6]$		$[-u_d / 3 - \sqrt{3}u_d / 3]$
Switch state																		
Vector	10	ONP	11	PNP	12	PN0	13	P00	14	ONN	15	PP0	16	00N	17	OP0	18	N0N
$[u_\alpha \ u_\beta]$		$[0 - \sqrt{3}u_d / 3]$		$[u_d / 3 - \sqrt{3}u_d / 3]$		$[u_d / 2 - \sqrt{3}u_d / 6]$		$[u_d / 3 \ 0]$		$[u_d / 3 \ 0]$		$[u_d / 6 \ \sqrt{3}u_d / 6]$		$[u_d / 6 \ \sqrt{3}u_d / 6]$		$[-u_d / 6 \ \sqrt{3}u_d / 6]$		$[-u_d / 6 \ \sqrt{3}u_d / 6]$
Switch state																		
Vector	19	OPP	20	N00	21	OOP	22	NN0	23	P0P	24	ON0	25	PPP	26	000	27	NNN
$[u_\alpha \ u_\beta]$		$[-u_d / 3 \ 0]$		$[-u_d / 3 \ 0]$		$[-u_d / 6 - \sqrt{3}u_d / 6]$		$[-vu_d / 6 - \sqrt{3}u_d / 6]$		$[u_d / 6 - \sqrt{3}u_d / 6]$		$[u_d / 6 - \sqrt{3}u_d / 6]$		$[0 \ 0]$		$[0 \ 0]$		$[0 \ 0]$
Switch state																		

FIGURE 3: Control set definition for a T-type three-level PCS.

based on an approximate prediction model. Then, use an accurate prediction model to predict the exact values of state variables in the next instant for all possible vectors within the down-sized control set.

- (5) Choose an appropriate cost function. Calculate the evaluation results for every possible vector.
- (6) Find the optimized value of cost function and the corresponding vector. Finally, set the semiconductor switches to the desired states according to the optimization result.

The beneficitions of proposed FCSMPC strategy compared to conventional method mainly include two aspects. First, the values of u_{cx} and i_{x2} are estimated based on state observer in Step 2. As a result, the corresponding sensors and sampling circuits can be omitted for purpose of decreasing the overall hardware cost. Second, the attempting

times decreases to no more than 7 after adopting the simplified calculation procedure proposed in this paper. As a comparison, 27 attempts must be made to find out the optimized vector in conventional FCSMPC implementations, which increase the calculation time-cost of processor. In Section 3, the implementation procedure of the proposed FCSMPC strategy will be introduced in detail.

3. Implementation Procedure of Proposed FCSMPC

3.1. Reference Generation. The control method of PCS can be carried out in $\alpha\beta$ reference frame based on the application of Clark transform. In most cases, active and reactive power are major instructions given by the upstream monitoring system. After receiving these instructions, they should be transferred to instantaneous voltage and current references

in $\alpha\beta$ frame first. For a three-phase system, active power P and reactive Q are expressed as

$$\begin{cases} p = \frac{3}{2}(u_{g\alpha} \times i_{g\alpha} + u_{g\beta} \times i_{g\beta}), \\ q = \frac{3}{2}(u_{g\beta} \times i_{g\alpha} - u_{g\alpha} \times i_{g\beta}). \end{cases} \quad (1)$$

$$\begin{bmatrix} i_{g\alpha}^*(k+1) \\ i_{g\beta}^*(k+1) \end{bmatrix} = \frac{2}{3(u_{g\alpha}^2(k+1) + u_{g\beta}^2(k+1))} \begin{bmatrix} u_{g\alpha}(k+1) & u_{g\beta}(k+1) \\ u_{g\beta}(k+1) & -u_{g\alpha}(k+1) \end{bmatrix} \begin{bmatrix} p^* \\ q^* \end{bmatrix}. \quad (2)$$

It is easy to deduce the reference value of u_{cx} and i_{x1} ($x = \alpha, \beta$) using the following equations:

$$\begin{bmatrix} u_{c\alpha}^* \\ u_{c\beta}^* \end{bmatrix} = \begin{bmatrix} u_{g\alpha} \\ u_{g\beta} \end{bmatrix} + \omega_{res} L_2 \begin{bmatrix} -i_{g\beta}^* \\ i_{g\alpha}^* \end{bmatrix}, \quad (3)$$

$$\begin{bmatrix} i_{\alpha 1}^* \\ i_{\beta 1}^* \end{bmatrix} = (1 - \omega_{res}^2 L_2 C) \begin{bmatrix} i_{\alpha 2}^* \\ i_{\beta 2}^* \end{bmatrix}. \quad (4)$$

Unfortunately, $u_{g\alpha}(k+1)$ and $u_{g\beta}(k+1)$ are not explicit variables in the k -th instant. It will lead to a delay for calculating the reference value if $u_{g\alpha}(k)$ and $u_{g\beta}(k)$ are directly substituted into equation (2) for an alternative choice. This delay will degrade the performance of PCS. To overcome this drawback, it is advisable to compensate the unit delay of grid voltage sampling conveniently based on predicting the voltage in the next instant using Lagrange extrapolation theorem [26]. $u_{gx}(k+1)$ calculated based on three-order Lagrange extrapolation is expressed as

$$u_{gx}(k+1) = 3u_{gx}(k) - 3u_{gx}(k-1) + u_{gx}(k-2) \quad x = \alpha, \beta. \quad (5)$$

3.2. Discrete-Time Prediction Model of LCL Filter-Based PCS. After accomplishing the reference calculation step, establishing the prediction model is also an important part for the control algorithm. It is apparent that the α -axis subsystem and β -axis subsystem are fully decoupled. Therefore, the model of the PCS based on LCL filter can be described by the state-space model given in the following equation:

$$\begin{cases} \dot{x}_\alpha = Ax_\alpha + B_i u_\alpha + B_g u_{g\alpha}, \\ \dot{x}_\beta = Ax_\beta + B_i u_\beta + B_g u_{g\beta}, \end{cases} \quad (6)$$

where the state spaces x_α and x_β are selected as

$$x_\alpha = [i_{\alpha 1} \quad i_{\alpha 2} \quad u_{c\alpha}]^T, \quad x_\beta = [i_{\beta 1} \quad i_{\beta 2} \quad u_{c\beta}]^T. \quad (7)$$

Expressions of matrix A , input matrix B_i , and B_g are given in the appendix. As the control method is

Hence, the reference of grid-injected current can be inversely deduced according to equation (2). The superscript of p^* and q^* denotes that those variables are reference signals.

usually implemented in a digital signal processor, the continuous-time state-space model needs to be converted to a discrete-time model by calculating the state transition equation first. By substituting sampling step time T_s into the continuous model, the PCS can be modelled as equation (8). The prediction step will be done using this discrete-time

$$\begin{cases} x_\alpha(k+1) = A_d x_\alpha(k) + B_{i d} u_\alpha(k) + B_{g d} u_{g\alpha}(k), \\ x_\beta(k+1) = A_d x_\beta(k) + B_{i d} u_\beta(k) + B_{g d} u_{g\beta}(k). \end{cases} \quad (8)$$

Matrices A_d , B_{id} , and B_{gd} are also given in the appendix. Furthermore, DC-link voltage balance is another important point in a three-level converter. Control algorithm should be adopted to guarantee the voltage balance of neutral point [27]. The difference between u_{dc1} and u_{dc2} should be considered to eliminate its negative impact on the power quality, especially for even-order harmonic performance of PCS. u_{dc1} and u_{dc2} can be expressed as follows:

$$\begin{cases} C_{dc} \frac{du_{dc1}}{dt} = i_{dc1}, \\ C_{dc} \frac{du_{dc2}}{dt} = i_{dc2}. \end{cases} \quad (9)$$

C_{dc} represents the capacitance of individual side capacitor. The difference of u_{dc1} and u_{dc2} , denoted as Δu_{dc} , varies according to

$$C_{dc} \frac{d\Delta u_{dc}}{dt} = C_{dc} \frac{d(u_{dc1} - u_{dc2})}{dt} = i_{dc1} - i_{dc2}. \quad (10)$$

The difference between i_{dc1} and i_{dc2} is denoted as i_{neu} . Then, we can deduce the relationship between Δu_{dc} and i_{neu} as

$$\Delta u_{dc} = \int \frac{(i_{dc1} - i_{dc2})}{C} dt = \int \frac{i_{neu}}{C} dt. \quad (11)$$

At last, i_{neu} can be obtained according to the switch state S_a , S_b , and S_c .

$$i_{neu} = (1 - |S_a|)i_a + (1 - |S_b|)i_b + (1 - |S_c|)i_c = -|S_a|i_a - |S_b|i_b - |S_c|i_c, \quad (12)$$

where S_x equals 1 when phase x ($x = a, b, c$) of the converter outputs positive voltage in “P” state, S_x equals 0 in “0” state, and S_x equals -1 in “N” state. For example, if operation state of converter is “PON” as shown in Figure 4(a), i_{neu} equals $-i_{a1} - i_{c1} = +i_{b1}$, if $i_{b1} > 0$, u_{dc1} will increase, and u_{dc2} will decrease; in contrast, u_{dc1} will increase and u_{dc2} will decrease if $i_{b1} < 0$. Figures 4(b) and 4(c) also illustrate the corresponding conditions when PCS generates “P00” and “0NN” vectors. It can be seen that P00 and 0NN vectors exert an opposite effect on Δu_{dc} .

Finally, we can get the following equation to predict Δu_{dc} in the next period as

$$\Delta u_{dc}(k+1) = \Delta u_{dc}(k) - \frac{T_s}{C_{dc}} (|S_a(k)|i_a(k) + |S_b(k)|i_b(k) + |S_c(k)|i_c(k)). \quad (13)$$

3.3. Simplified Optimization Strategy. For conventional FCSMPC strategy, 27 different vectors need to be substituted separately to the aforementioned mathematical model. However, only a minor part of the complete control set is possible to be the candidate vectors and should participate in the cost function calculation step in one specific control period. In order to reduce the computation burden, most vectors far from the optimized vector can be excluded easily by a rough estimation before the accurate prediction model is executed.

For this reason, if the capacitors in the LCL filter are assumed to be nonexistent first, a rough estimation of output vector can be deduced in the same way as continuous control state model predictive control in a single L filter (assuming $L = L_1 + L_2$) based converter. In this case, the approximately estimated output voltage of PCS, denoted as $u_{\alpha E}$ and $u_{\beta E}$, can be obtained as given in equation (14).

$$\begin{cases} u_{\alpha E}(k+1) = L \times (i_{\alpha 2}^*(k+1) - i_{\alpha 1}(k)) + T_s \times \frac{u_{g\alpha}(k)}{T_s}, \\ u_{\beta E}(k+1) = \frac{[L \times (i_{\beta 2}^*(k+1) - i_{\beta 1}(k)) + T_s \times u_{g\beta}(k)]}{T_s}. \end{cases} \quad (14)$$

Apparently, the values of $u_{\alpha E}$ and $u_{\beta E}$ are very likely unequal to any vector that the converter can generate directly. However, the optimized vector must locate in the vicinity of $u_{\alpha E}$ and $u_{\beta E}$. That is to say, only the vectors near ($u_{\alpha E}$, $u_{\beta E}$) are possible candidates for the next switch period. The other vectors can be discarded in the further optimization process. For example, if $u_{\alpha E} = 0.5u_{bat}$, $u_{\beta E} = 0.1u_{bat}$, the optimized vector will only be selected from the subset of PNN, P0N PPN and 00P according to Figure 2. Therefore, how to judge which vectors are the nearest ones to the ($u_{\alpha E}$, $u_{\beta E}$) as fast as possible is essential to simplify the algorithm to reduce the computation burden of digital controller. For this purpose, intermediate integers a , b , and c are defined as

$$\begin{cases} a = \text{sign}(u_{\alpha E}), \\ b = \text{sign}(\sqrt{3}u_{\beta E} - u_{\alpha E}), \\ c = \text{sign}(-\sqrt{3}u_{\beta E} - u_{\alpha E}). \end{cases} \quad (15)$$

Function $\text{sign}(y)$ returns the polarity of input number y . If $y > 0$, $\text{sign}(y)$ equals 1; otherwise, $\text{sign}(x)$ returns 0. After that, the origin of $\alpha\beta$ plane can be referenced to one of the six vertices of small vectors. Based on this method, complicated three-level modulation can be reduced to a two-level one. We can get the relationship between modified $u_{\alpha m}$, $u_{\beta m}$, and original signals as

$$\begin{cases} u_{\alpha m} = u_{\alpha E} - u_{\alpha 0}, \\ u_{\beta m} = u_{\beta E} - u_{\beta 0}. \end{cases} \quad (16)$$

From the above equations, $u_{\alpha 0}$ and $u_{\beta 0}$ can be obtained:

$$\begin{cases} u_{\alpha 0} = \frac{1}{3}a - \frac{1}{6}b - \frac{1}{6}c, \\ u_{\beta 0} = \frac{\sqrt{3}}{6}(b - c). \end{cases} \quad (17)$$

After redefining the virtual origin point, the vector location in one hexagon should be deduced. In order to achieve this goal, auxiliary integers d , e , and f are defined as

$$\begin{cases} d = \text{sign}(u_{\beta m}), \\ e = \text{sign}(\sqrt{3}u_{\alpha m} - u_{\beta m}), \\ f = \text{sign}(-\sqrt{3}u_{\alpha m} - u_{\beta m}). \end{cases} \quad (18)$$

On the basis of equation (18), a new integer N is defined as

$$N = d + 2e + 4f. \quad (19)$$

By calculating the value of a , b , c , and N , the location of ($u_{\alpha m}$, $u_{\beta m}$) in a hexagon can be deduced as shown in Figure 5. Meanwhile, Table 1 lists the possible candidate vectors for exhaustive conditions.

Then, the respective vectors are substituted to the accurate predictive model given from equation (6) to equation (13), aiming to choose the best vector which will become active in the next period. After using this method, only 5–7 vectors are necessary to be considered in the accurate calculation step. This is helpful to largely decrease the calculation time consumption of the PCS compared to traditional model predictive control algorithm. Note that, in fact, it is needless to calculate all three zero vectors in prediction. If the possibly chosen vector in the next period is zero vector, these zero vectors impact the grid current and DC voltage in the same way. Therefore, the optimized vector is chosen to be the one which can decrease the switching frequency to the lowest. For example, if the last state is “PP0”, “PPP” will be chosen since only S_{c1} and S_{c3} participate in switching over process in this case.

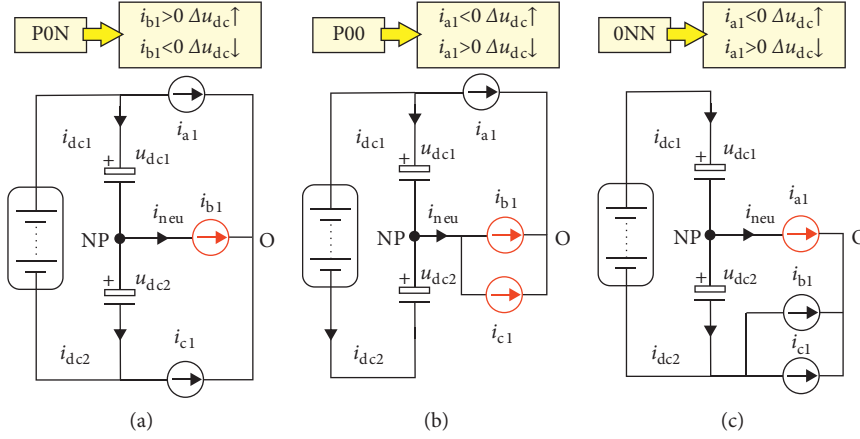
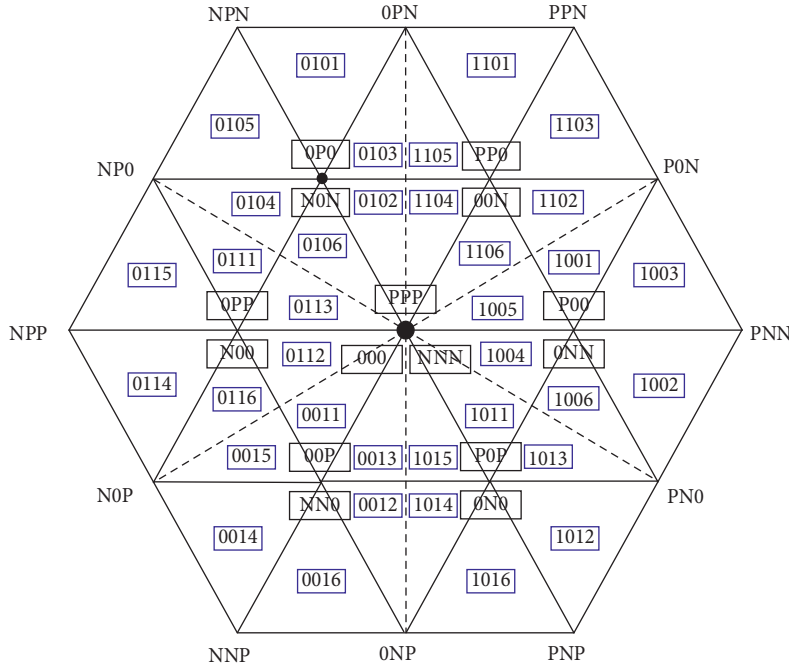


FIGURE 4: Effects of different vectors on neutral point current. (a) P0N case. (b) P00 case. (c) 0NN case.


 FIGURE 5: An index diagram from auxiliary integer values to the location of point $(u_{\alpha E}, u_{\beta E})$.

3.4. Full-Dimensional State Observer. To avoid the additional nonessential sensors, full-dimensional state observers are adopted. The configuration of continuous-time based state observer for α -axis components is shown in Figure 6. The β -axis observer has the same structure as α -axis. The α -axis state observer is modelled in continuous-time domain as

$$\dot{\hat{x}}_{\alpha} = A\hat{x}_{\alpha} + B_i u_{\alpha} + B_g u_{g\alpha} + KC(x_{\alpha} - \hat{x}_{\alpha}). \quad (20)$$

Because $i_{\alpha 1}$ and $i_{\beta 1}$ are indispensable variables directly probed by current sensors in PCS control, they are chosen to construct the feedback loop of state observer by setting output matrix C to $[1 \ 0 \ 0]^T$. In order to verify the feasibility of state observer, the observability should be certified first.

As can be seen in equation (21), the rank of observability matrix equals 3, which is full ranked, indicating that it is possible to estimate all the state variables in the α -axis subsystem. Based on the same principle, the variables in the β -axis subsystem are also estimated in the same way as α -axis subsystem.

$$\text{rank}[C \ CA \ CA^2]^T = 3. \quad (21)$$

Matrix K performs as the feedback gain matrix to calibrate the observed values to the real values in the physical system. By adjusting K , the eigenvalues of observer can be arbitrarily designed.

$$K = [K_1 \ K_2 \ K_3]^T. \quad (22)$$

TABLE 1: Selection guide for candidate vectors based on a , b , c , and N .

$[a, b, c, N]$	Candidate vector
1001	P0N P00 0NN PPO 00N
1002	PNN PNO P00 0NN
1003	PNN P0N P00 0NN
1004	P00 0NN POP 0NO (PPP 000 NNN)
1005	P00 0NN PPO 0NN (PPP 000 NNN)
1006	PNO P00 0NN POP 0NO
1101	PPN 0PN PPO 00N
1102	P0N P00 0NN PPO 00N
1103	P0N PPN PPO 00N
1104	PPO 00N 0PO N0N (PPP 000 NNN)
1105	PP0 00N 0PN 0P0 N0N
1106	P00 0NN PPO 00N (PPP 000 NNN)
0101	0PN NPN 0P0 N0N
0102	PPO 00N 0PO N0N (PPP 000 NNN)
0103	0PN PPO 00N 0P0 N0N
0104	NPO 0P0 N0N 0PP N00
0105	NPN NPO 0P0 N0N
0106	0P0 N0N 0PP N00 (PPP 000 NNN)
0111	NPO 0P0 N0N 0PP N00
0112	0PP N00 00P NNO (PPP 000 NNN)
0113	0P0 N0N 0PP N00 (PPP 000 NNN)
0114	NPP N0P 00P N00
0115	NPO NPP 0PP N00
0116	N0P 0PP N00 00P NNO
0011	0PP N00 00P NNO (PPP 000 NNN)
0012	0NP 00P NNO POP 0NO
0013	00P NNO POP 0NO (PPP 000 NNN)
0014	N0P NNP 00P NNO
0015	N0P 0PP N00 00P NNO
0016	NNP 0NP 00P NNO
1011	P00 0NN POP 0NO (PPP 000 NNN)
1012	PNP PNO POP 0NO
1013	PNO P00 0NN POP 0NO
1014	0NP 00P NNO POP 0NO
1015	00P NNO POP 0NO (PPP 000 NNN)
1016	0NP PNP POP 0NO

The response of observation error Δx_α will vary according to the calibration parameters setting.

$$\Delta \hat{x}_\alpha(t) = e^{(A-KC)t} \Delta \hat{x}_\alpha(0). \quad (23)$$

To guarantee the convergence of observation error, the eigenvalue of $A - KC$ is very important. The characteristic polynomial of $A - KC$ is given by

$$\det(sI - A + KC) = s^3 + K_1 s^2 + \frac{L_1 + L_2 - L_2 CK_3}{L_1 L_2 C} s + \frac{K_1 L_1 + K_2 L_2}{L_1 L_2 C} = 0. \quad (24)$$

The root of characteristic polynomial should all locate in the left half complex plane to avoid an unstable condition; otherwise, the observation error will diverge to infinity. By applying Routh criterion, we can deduce the parameter $K_1 \sim K_3$ should satisfy the rule as follows:

$$\begin{cases} K_1 > 0, \\ K_1 L_1 + K_2 L_2 > 0, \\ K_3 < \frac{L_1 + L_2}{L_2 C}, \\ K_1 - K_1 K_3 C > K_2. \end{cases} \quad (25)$$

After the feedback parameters are determined, it is easy to implement the state observer in a digital controller by utilizing a general discretization solution such as backward-Euler method.

3.5. Cost Function. Finally, the cost function should be chosen properly to finish the whole algorithm. This is the vital step in FCSMPC. In order to approach the control of both output current and NP balance, the cost function in this paper is chosen to be

$$J = \varepsilon_{i1}^2 + \lambda_{i2} \varepsilon_{i2}^2 + \lambda_u \varepsilon_u^2 + \lambda_{udc} \Delta U_{dc}(k+1)^2, \quad (26)$$

where λ_{i1} , λ_{i2} , λ_u , and λ_{udc} represent the weighing factors to adjust the priority of control objective. ε_{i1} , ε_{i2} , and ε_u represent the errors between reference and predicted value in the next instant. Their expressions are given by

$$\begin{cases} \varepsilon_{i1} = (i_{\alpha 1}^*(k+1) - i_{\alpha 1}(k+1))^2 + (i_{\beta 1}^*(k+1) - i_{\beta 1}(k+1))^2, \\ \varepsilon_{i2} = (i_{\alpha 2}^*(k+1) - i_{\alpha 2}(k+1))^2 + (i_{\beta 2}^*(k+1) - i_{\beta 2}(k+1))^2, \\ \varepsilon_u = (u_{ca}^*(k+1) - u_{ca}(k+1))^2 + (u_{cb}^*(k+1) - u_{cb}(k+1))^2. \end{cases} \quad (27)$$

By substituting the predictive results in the cost function, the appropriate vector corresponding to the minimum value of J can be selected to be sent out by the PCS to form the optimized grid-injected current.

4. Simulation and Experimental Results

In order to evaluate the feasibility of PCS applied in BESS based on the simplified control algorithm proposed in this paper, simulation study is performed based on MATLAB/Simulink. Then, experimental research studies are also carried out. The diagram of simulation model is shown in Figure 7. Its main electric parameters are listed in Table 2.

First, the steady state performance of PCS is verified by setting active power reference to 2300 W. Meanwhile, reactive power reference is forced to be zero to achieve unity power operation. The simulation waveforms are shown in Figures 8(a)–8(c). It can be seen that the output voltage per one phase leg of 3L-VSC has three states and line voltage has five states according to Figure 8(a). The grid-injected current possesses the same frequency and phase angle with grid voltage, which certifies that power factor (PF) is equal to 1.0. The three-phase waveforms of grid-side voltage and current

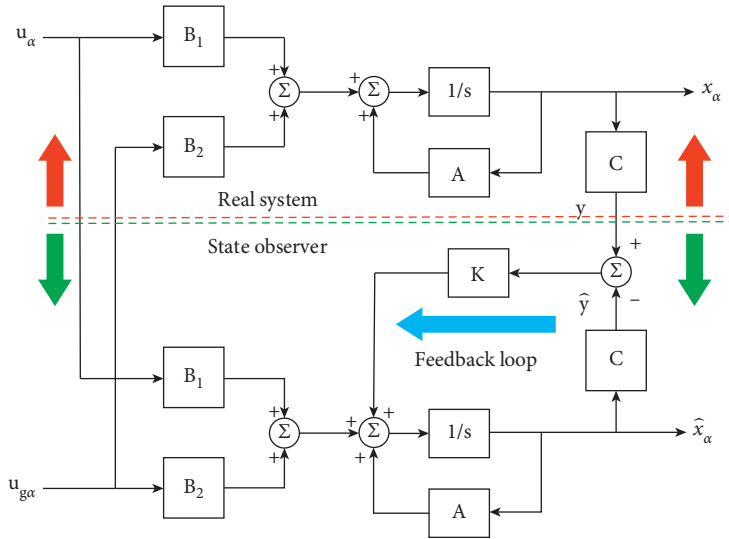


FIGURE 6: Structure of α -axis full-dimensional state observer.

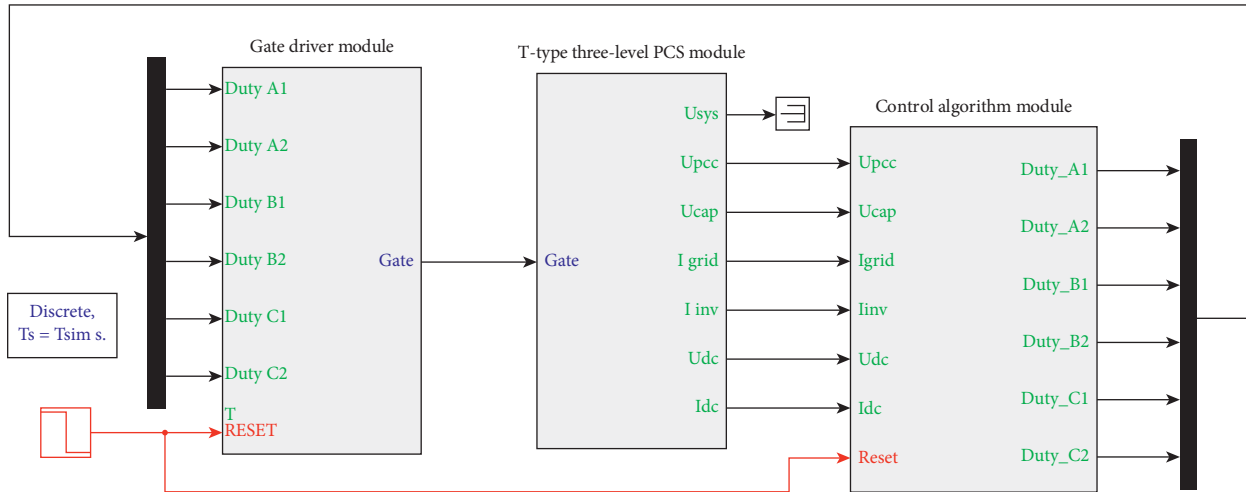


FIGURE 7: Simulation model diagram of PCS based on MATLAB/Simulink.

TABLE 2: Main electric parameters for the simulation model of PCS.

Parameter	Value	Unit
Rated power	2300	VA
Nominal total DC-link voltage	360	V _{dc}
Nominal grid voltage (phase to phase)	110	V _{rms}
Nominal grid frequency	50.0	Hz
Sampling frequency	30.0	kHz
Inductance of L_1	3.6	mH
Inductance of L_2	1.2	mH
Filtering capacitance of C	3.3	μ F
DC-link capacitance of C_{dc}	4.7	mF

are illustrated in Figure 8(b). The amplitude of symmetric grid current is 10 A. This corresponds exactly to the power reference. Moreover, it is possible to adjust the power factor by setting reactive power to different values. In Figure 8(c), the grid voltage is leading to current by approximately 25°

after setting reactive power reference to 1100 Var. PF is 0.9 in this case. Power factor can accurately follow the command. As a supplement, the similar test is carried out for battery-charging operation. Figures 9(a)–9(c) show the simulation waveforms.

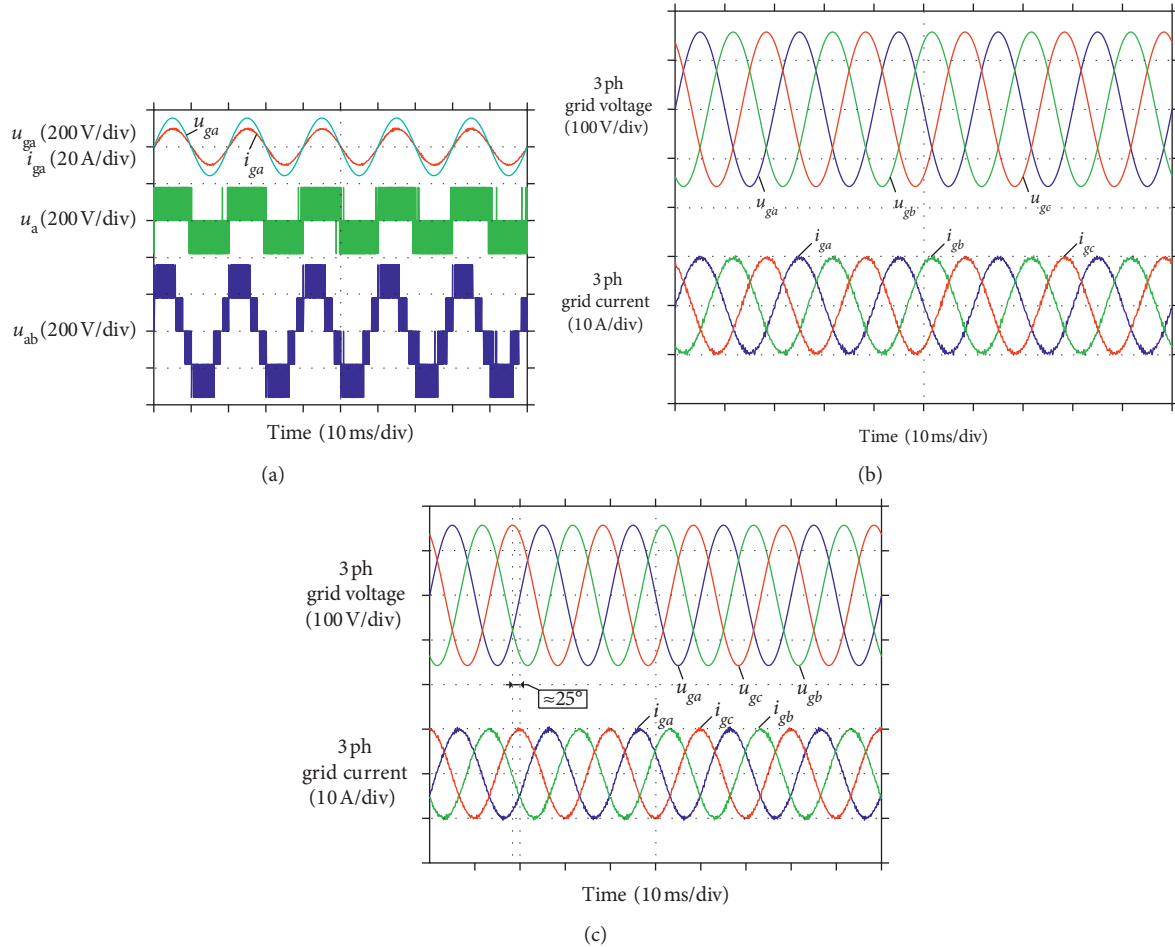


FIGURE 8: Simulation results of PCS in full load battery-discharging condition. (a) Waveforms of u_{ga} , i_{ga} , u_a , and u_{ab} (PF = 1.0). (b) Waveforms of three-phase grid voltage and current (PF = 1.0). (c) Waveforms of three-phase grid voltage and current (PF = 0.9).

The dynamic performance of the proposed control strategy is tested by executing a full power transition between charging and discharging conditions. Figure 10(a) shows the simulated transient response when PCS changes from discharging operation to charging operation at rated power. Furthermore, Figure 10(b) shows the simulated transient response when PCS changes from charging to discharging condition. It can be seen that both dynamic processes end in about 5 ms, which can meet the responding speed requirement in most situations.

For the three-level energy conversion topology with split dc-link capacitors, the balance of dc-link is very important. Therefore, the effect of the DC voltage equalization control implemented integrated within FCSMPC is also tested based on the simulation model. Figure 11 shows the simulation results to make a comparison of control algorithm with and without NP balance strategy. At the beginning of simulation, the balance algorithm is shut down by setting λ_{udc} to zero until 200 ms. After activating the balance algorithm, we can find that the diverging DC voltages u_{dc1} and u_{dc2} start to converge again. Finally, u_{dc1} approximately equals u_{dc2} . On

the basis of simulation results, we can conclude that the DC-link is well balanced.

Then, the performance of state observer is further tested. Figure 12(a) compares the actual and estimated value of $i_{g\alpha}$ and $i_{g\beta}$ in discharging situation. Meanwhile, Figure 12(b) compares the estimated and actual value of filter capacitor's voltage in $\alpha\beta$ reference frame. Figures 12(c) and 12(d) give similar simulation results during charging operation state. On the basis of these simulation results, the convergence of observer can be confirmed. Because of the numerical similarity between actual and estimated values, it is feasible to replace the actual values with the estimated values extracted from the observer.

Finally, in some specific applications, PCS needs to deal with the issue to connect into unbalanced grid. Therefore, it is necessary to verify the ability of the proposed control method to resist the negative impact of nonideal grid. Figures 13(a) and 13(b) show the simulation results for PCS when it is connected to unbalanced grid. Both discharging and charging conditions are taken into account in the simulation. We can see that the PCS works normally in this

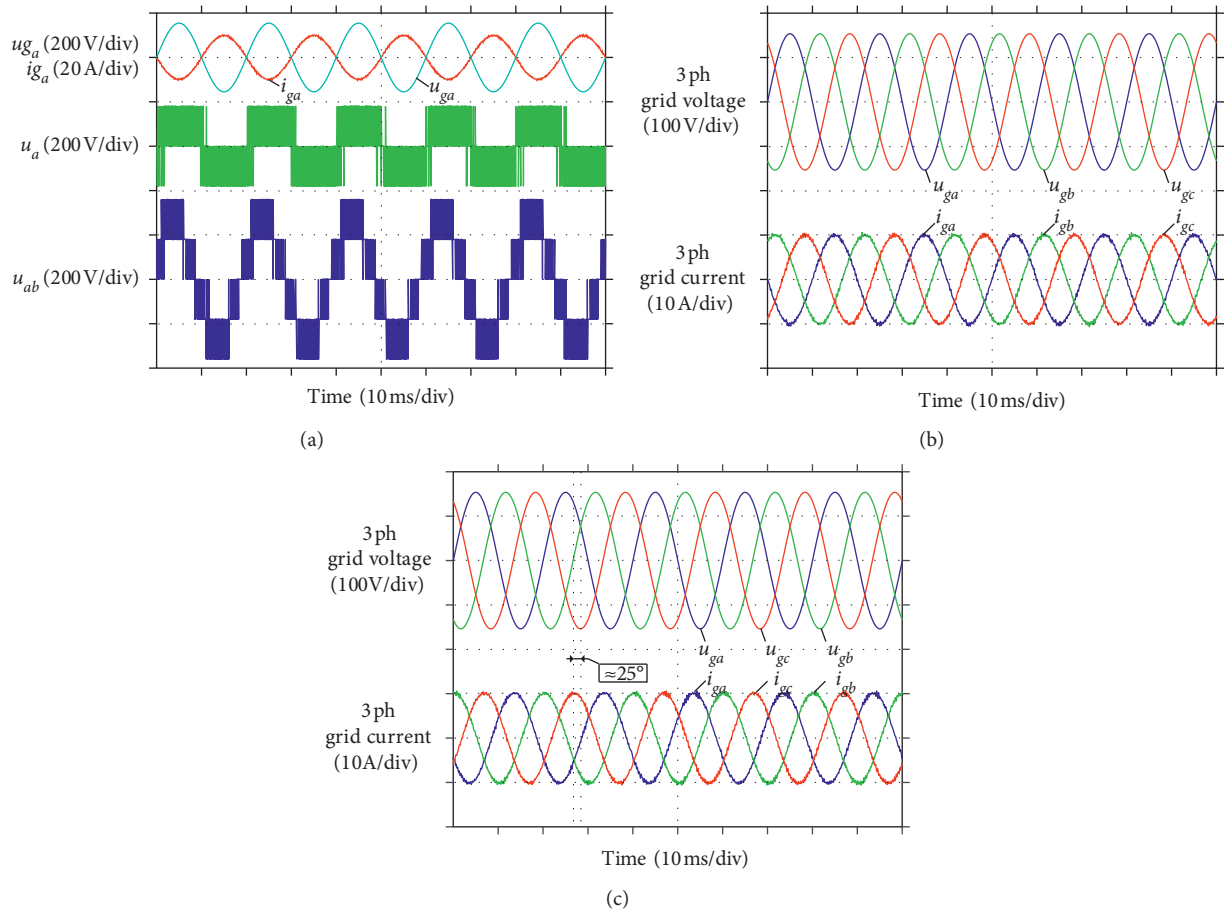


FIGURE 9: Simulation results of PCS in full load battery-charging condition. (a) Waveforms of u_{ga} , i_{ga} , u_a , and u_{ab} (PF = 1.0). (b) Waveforms of three-phase grid voltage and current (PF = 1.0). (c) Waveforms of three-phase grid voltage and current (PF = 0.9).

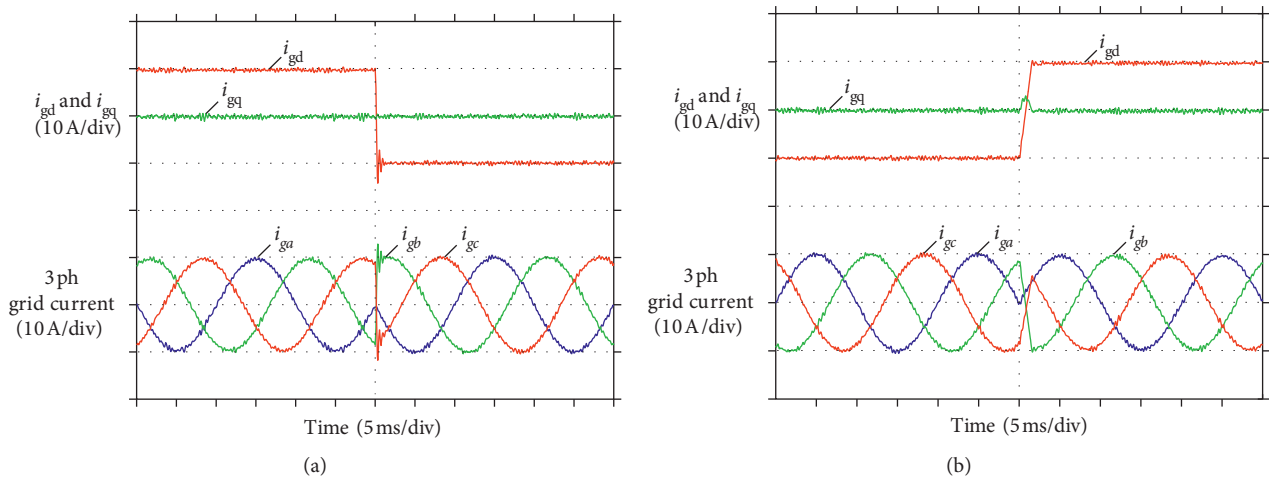


FIGURE 10: Simulation results of PCS in dynamic Process. (a) Waveforms of grid current both in dq and abc reference frame for transition from full load discharging to charging operation. (b) Waveforms of grid current both in dq and abc reference frame for transition from full load charging to discharging operation.

case. Power quality of the grid-injected current is acceptable even if three-phase grid voltage is asymmetric.

For purpose of further verifying the correctness of theoretical analysis and control algorithm, a T-type 3L PCS

experimental platform is constructed in the laboratory and a series of tests are carried out based on the prototype. The parameters of prototype are identical to the simulation model which has been given in Table 2. Figure 14 shows the

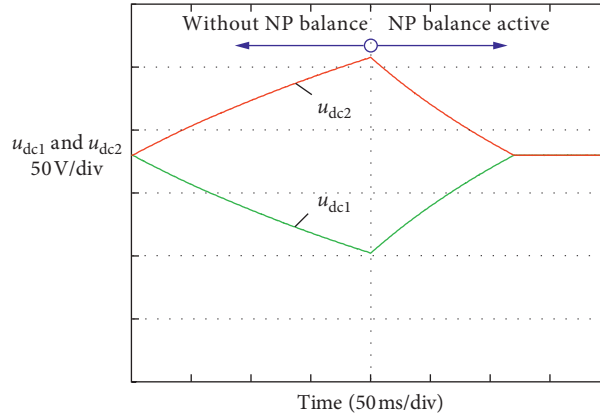


FIGURE 11: Simulation results of DC-link voltage with and without NP balance algorithm.

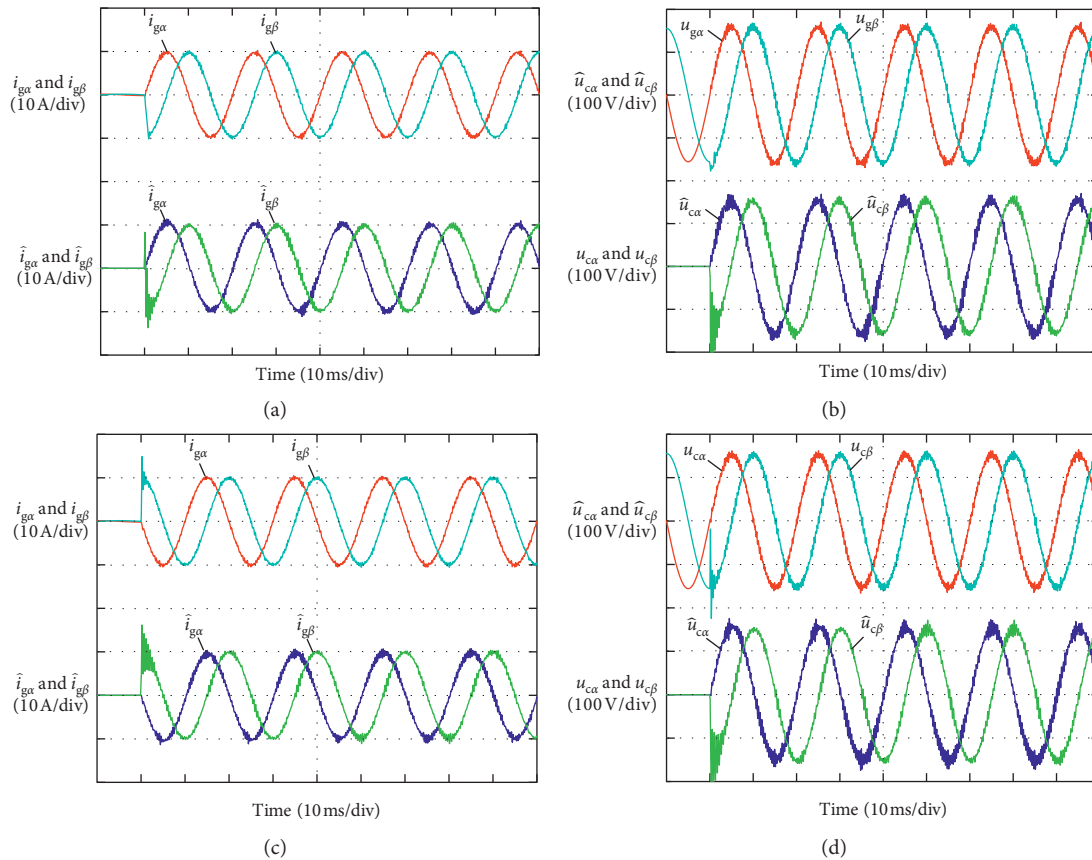


FIGURE 12: Simulation results of full-dimensional state observers. (a) Waveforms of actual and estimated grid current when PCS is discharging. (b) Waveforms of actual and estimated capacitor voltage when PCS is discharging. (c) Waveforms of actual and estimated grid current when PCS is charging. (d) Waveforms of actual and estimated capacitor voltage when PCS is charging.

photo of prototype. IKW40T120 IGBTs are chosen to be the main switches (S_{x1} and S_{x4}). FGA40N65SMD IGBTs are chosen to be the auxiliary switches (S_{x2} and S_{x3}). Driving circuits of these semiconductor switches are based on 1EDI20I12AF. TMS320F28335 performs as the main digital controller. DC terminals of the prototype are connected to the programmable DC power supply Chroma

62150H-600S. The grid voltage is emulated by programmable AC power supply Chroma 61830 and provided to the AC terminals of the prototype. A GWinstek MDO2204ES oscilloscope is used to capture the voltage and current signals.

First, the steady state performance of T-type 3L PCS is tested and verified. The waveforms obtained based on the

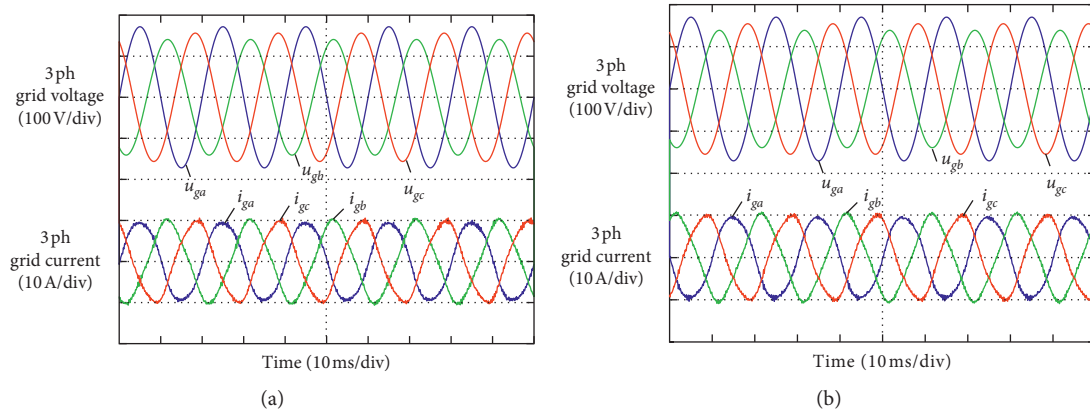


FIGURE 13: Simulation results of PCS connected to a nonideal grid. (a) Three-phase grid voltage and current in battery-discharging condition. (b) Three-phase grid voltage and current in battery-charging condition.

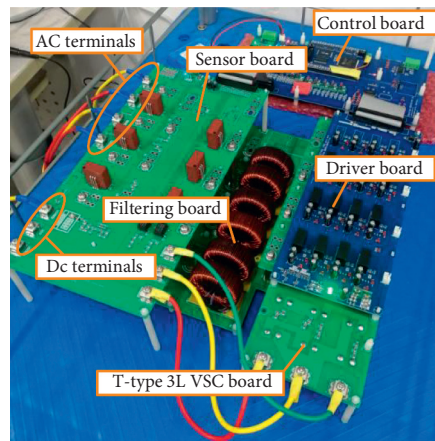


FIGURE 14: Photo of the experimental platform.

prototype are shown in Figure 15. Figures 15(a) and 15(b) show the testing results for nominal battery discharging and charging operation at rated power. We can see that the grid-injected current is mostly sinusoidal and maintains the same phase angle and frequency as grid voltage to guarantee a unity power factor operation. If the power factor is not equal to 1.0, the PCS is able to provide or absorb reactive power as required to/from the grid. Figures 15(c) and 15(d) depict the measured waveforms in such cases by setting commanded reactive power to ± 1100 VA. It can be seen that an apparent phase difference (approximately 25°) arises between the voltage and current signals. Figure 15(e) shows the output line voltage of T-type 3L PCS. The line voltage has five levels. Therefore, it contains fewer voltage harmonics compared to 2L PCS. The experimental results in Figure 15 are evident to confirm the correctness and feasibility of the control algorithm discussed in this paper.

After that, a series of experiments to verify the dynamic performance of PCS prototype based on the proposed control method are carried out. Figure 16(a) shows the acquired grid voltage and current waveforms when PCS starts to discharge at rated power. Similarly, Figure 16(b) illustrates the measured grid voltage and current waveforms when PCS starts to charge at rated power. It can be deduced that the start-up process of PCS is stable and fast without significant oscillation or overshoot. Figure 16(c) depicts the transient response when PCS suddenly changes from discharging operation to charging operation both at rated power. Figure 16(d) shows the transient response for a reverse transition. It can be found the transient affairs end up within less than half a grid cycle, which is acceptable for most industrial energy storage applications. We can see that the experimental results are in good agreement with the simulation results, which can verify the correctness of the algorithm proposed in this paper.

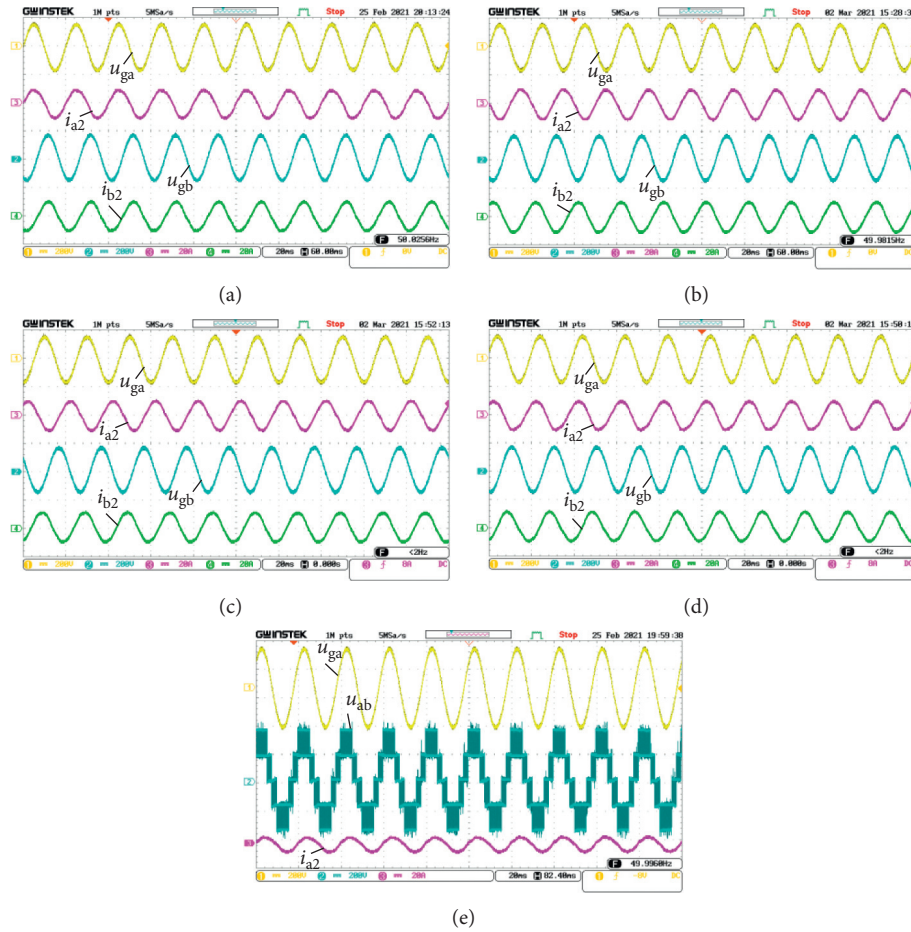


FIGURE 15: Experimental results of the PCS prototype. (a) Grid voltage and current waveforms in battery-discharging condition (unity PF). (b) Grid voltage and current waveforms in battery-charging condition (unity PF). (c) Grid voltage and current waveforms in battery-discharging condition ($|PF| = 0.9$). (d) Grid voltage and current waveforms in battery-charging condition ($|PF| = 0.9$). (e) Output line voltage waveforms of T-type 3L PCS.

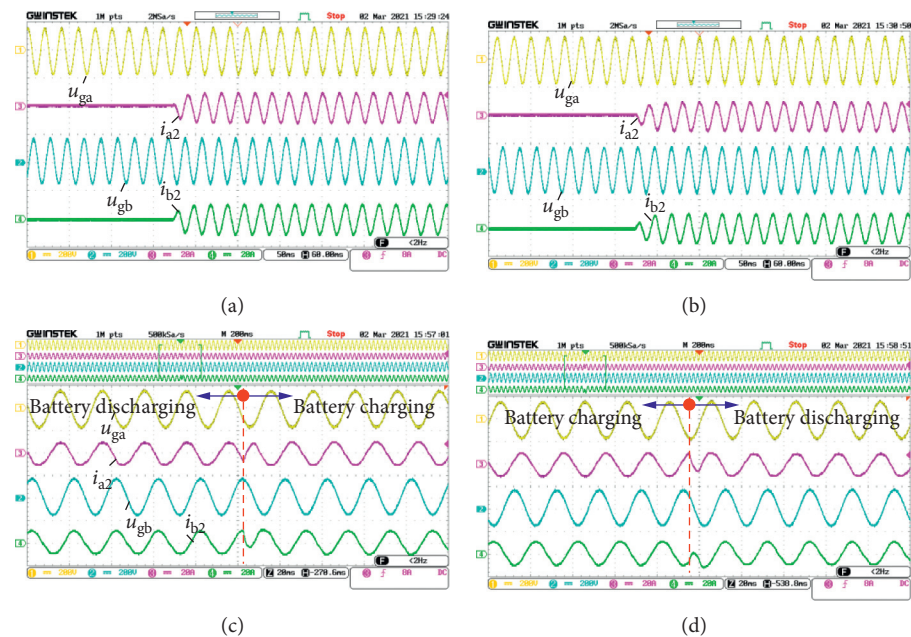


FIGURE 16: Experimental results of the PCS prototype. (a) Grid voltage and current waveforms for nominal discharging start-up test. (b) Grid voltage and current waveforms for nominal charging start-up test. (c) Transient waveforms when PCS changes from discharging to charging condition. (d) Transient waveforms when PCS changes from charging to discharging condition.

5. Conclusions

This paper proposes a simplified FCSMPC strategy for T-type three-level PCS applied in BESS. The simplification is reflected in two aspects: (1) simplify the algorithm by a two-step predictive calculation to decrease the overall calculation complexity; (2) simplify the sensors and sampling circuits by adopting full-dimensional state observer to estimate capacitor voltage and grid current. Moreover, the observer is able to estimate the variables correctly, which makes it

possible to save several sensors in the main circuit. According to the simulation and experimental results, we can conclude that the proposed control strategy is feasible and effective. The steady state and dynamic performance of PCS based on the modified control method is reliable for either charging or discharging operating conditions.

Appendix

The matrices in Section 3 are defined as follows:

$$\begin{aligned}
 A &= \begin{bmatrix} 0 & 0 & \frac{-1}{L_1} \\ 0 & 0 & \frac{1}{L_2} \\ \frac{1}{C} & \frac{-1}{C} & 0 \end{bmatrix}, B_i = \begin{bmatrix} \frac{1}{L_1} \\ 0 \\ 0 \end{bmatrix}, B_g = \begin{bmatrix} 0 \\ \frac{-1}{L_2} \\ 0 \end{bmatrix}, \\
 A_d = e^{AT_s} &= \begin{bmatrix} \frac{L_1 + L_2 \cos(\omega_{\text{res}} T_s)}{L_1 + L_2} & \frac{L_2 - L_2 \cos(\omega_{\text{res}} T_s)}{L_1 + L_2} & -\frac{\sin(\omega_{\text{res}} T_s)}{\omega_{\text{res}} L_1} \\ \frac{L_1 - L_1 \cos(\omega_{\text{res}} T_s)}{L_1 + L_2} & \frac{L_2 + L_1 \cos(\omega_{\text{res}} T_s)}{L_1 + L_2} & \frac{\sin(\omega_{\text{res}} T_s)}{\omega_{\text{res}} L_2} \\ \frac{\sin(\omega_{\text{res}} T_s)}{\omega_{\text{res}} C} & -\frac{\sin(\omega_{\text{res}} T_s)}{\omega_{\text{res}} C} & \cos(\omega_{\text{res}} T_s) \end{bmatrix}, \\
 B_{id} = \int_0^{T_s} e^{A\tau} B_i d\tau &= \begin{bmatrix} \frac{T_s}{L_1 + L_2} + \frac{L_2 \sin(\omega_{\text{res}} T_s)}{L_1 (L_1 + L_2) \omega_{\text{res}}} \\ \frac{T_s}{L_1 + L_2} - \frac{\sin(\omega_{\text{res}} T_s)}{(L_1 + L_2) \omega_{\text{res}}} \\ \frac{L_2 (1 - \cos(\omega_{\text{res}} T_s))}{(L_1 + L_2)} \end{bmatrix},
 \end{aligned} \tag{A.1}$$

where

$$\omega_{\text{res}} = \sqrt{\frac{L_1 + L_2}{L_1 L_2 C}}. \tag{A.2}$$

Data Availability

The data used to support the findings of this study are available from the corresponding author upon request.

Conflicts of Interest

The authors declare that they have no conflicts of interest.

Acknowledgments

This research was supported by National Natural Science Foundation of China (no. 51907119) and Shanghai Sailing Program (no. 19YF1418700).

References

- [1] M. Fan, K. Sun, D. Lane, W. Gu, Z. Li, and F. Zhang, "A novel generation rescheduling algorithm to improve power system reliability with high renewable energy penetration," *IEEE Transactions on Power Systems*, vol. 33, no. 3, pp. 3349–3357, 2018.
- [2] C. Zhang, X. Cai, A. Rygg, and M. Molinas, "Sequence domain SISO equivalent models of a grid-tied voltage source converter

- system for small-signal stability analysis," *IEEE Transactions on Energy Conversion*, vol. 33, no. 2, pp. 741–749, 2018.
- [3] J. P. Barton and D. G. Infield, "Energy storage and its use with intermittent renewable energy," *IEEE Transactions on Energy Conversion*, vol. 19, no. 2, pp. 441–448, 2004.
 - [4] S. Vazquez, S. M. Lukic, E. Galvan et al., "Energy storage systems for transport and grid applications," *IEEE Transactions on Industrial Electronics*, vol. 57, no. 12, pp. 3881–3895, 2011.
 - [5] Y. Ma, W. Cao, L. Yang, F. F. Wang, and L. M. Tolbert, "Virtual synchronous generator control of full converter wind turbines with short-term energy storage," *IEEE Transactions on Industrial Electronics*, vol. 64, no. 11, pp. 8821–8831, 2017.
 - [6] K. C. Divya and J. Østergaard, "Battery energy storage technology for power systems-An overview," *Electric Power Systems Research*, vol. 79, no. 4, pp. 511–520, 2009.
 - [7] Y. Y. Leow, C. A. Ooi, and M. N. Hamidi, "Performance evaluation of grid-connected power conversion systems integrated with real-time battery monitoring in a battery energy storage system," *Electrical Engineering*, vol. 102, no. 1, pp. 245–258, 2020.
 - [8] S. Alepuz, S. Busquets-Monge, J. Bordonau, J. Gago, D. Gonzalez, and J. Balcells, "Interfacing renewable energy sources to the utility grid using a three-level inverter," *IEEE Transactions on Industrial Electronics*, vol. 53, no. 5, pp. 1504–1511, 2006.
 - [9] A. Nabae, I. Takahashi, and H. Akagi, "A new neutral-point-clamped PWM inverter," *IEEE Transactions on Industry Applications*, vol. IA-17, no. 5, pp. 518–523, 1981.
 - [10] Y. Jiao and F. C. Lee, "New modulation scheme for three-level active neutral-point-clamped converter with loss and stress reduction," *IEEE Transactions on Industrial Electronics*, vol. 62, no. 9, pp. 5468–5479, 2015.
 - [11] C. Liu, X. Cai, and Q. Chen, "Self-adaptation control of second-life battery energy storage system based on cascaded H-bridge converter," *IEEE Journal of Emerging and Selected Topics in Power Electronics*, vol. 8, no. 2, pp. 1428–1441, 2020.
 - [12] H. Chen, C. Lu, and W. Lien, "Active capacitor voltage balancing control for three-level flying capacitor boost converter," in *Proceedings of the Applied Power Electronics Conference and Exposition (APEC)*, pp. 127–132, San Antonio, TX, USA, May 2018.
 - [13] M. Schweizer and J. W. Kolar, "Design and implementation of a highly efficient three-level T-type converter for low-voltage applications," *IEEE Transactions on Power Electronics*, vol. 28, no. 2, pp. 899–907, 2013.
 - [14] R. Peña-Alzola, M. Liserre, F. Blaabjerg, M. Ordonez, and T. Kerekes, "A self-commissioning notch filter for active damping in a three-phase LCL -Filter-Based grid-tie converter," *IEEE Transactions on Power Electronics*, vol. 29, no. 12, pp. 6754–6761, 2014.
 - [15] S. Kouro, P. Cortes, R. Vargas, U. Ammann, and J. Rodriguez, "Model predictive control-A simple and powerful method to control power converters," *IEEE Transactions on Industrial Electronics*, vol. 56, no. 6, pp. 1826–1838, 2009.
 - [16] A. Dekka, B. Wu, V. Yaramasu, R. L. Fuentes, and N. R. Zargari, "Model predictive control of high-power modular multilevel converters-an overview," *IEEE Journal of Emerging and Selected Topics in Power Electronics*, vol. 7, no. 1, pp. 168–183, 2019.
 - [17] P. Falkowski and A. Sikorski, "Finite control set model predictive control for grid-connected AC-DC converters with LCL filter," *IEEE Transactions on Industrial Electronics*, vol. 65, no. 4, pp. 2844–2852, 2018.
 - [18] Y. Yang, H. Wen, M. Fan, M. Xie, and R. Chen, "Fast finite-switching-state model predictive control method without weighting factors for T-type three-level three-phase inverters," *IEEE Transactions on Industrial Informatics*, vol. 15, no. 3, pp. 1298–1310, 2019.
 - [19] X. Liu, D. Wang, and Z. Peng, "A computationally efficient FCS-MPC method without weighting factors for NNPCs with optimal duty cycle control," *IEEE/ASME Transactions on Mechatronics*, vol. 23, no. 5, pp. 2503–2514, 2018.
 - [20] C. Xia, T. Liu, T. Shi, and Z. Song, "A simplified finite-control-set model-predictive control for power converters," *IEEE Transactions on Industrial Informatics*, vol. 10, no. 2, pp. 991–1002, 2014.
 - [21] M. Habibullah, D. D.-C. Lu, D. Xiao, and M. F. Rahman, "A simplified finite-state predictive direct torque control for induction motor drive," *IEEE Transactions on Industrial Electronics*, vol. 63, no. 6, pp. 3964–3975, 2016.
 - [22] M. Malinowski and S. Bernet, "A simple voltage sensorless active damping scheme for three-phase PWM converters with an $\$LCL\$$ filter," *IEEE Transactions on Industrial Electronics*, vol. 55, no. 4, pp. 1876–1880, 2008.
 - [23] X. Wang, F. Blaabjerg, and P. C. Loh, "Grid-current-feedback active damping for LCL resonance in grid-connected voltage-source converters," *IEEE Transactions on Power Electronics*, vol. 31, no. 1, pp. 213–223, 2016.
 - [24] J. Kukkola and M. Hinkkanen, "State observer for grid-voltage sensorless control of a converter under unbalanced conditions," *IEEE Transactions on Industry Applications*, vol. 54, no. 1, pp. 286–297, 2018.
 - [25] J. M. Kanieski, R. Cardoso, H. Pinheiro, and H. A. Gründling, "Kalman filter-based control system for power quality conditioning devices," *IEEE Transactions on Industrial Electronics*, vol. 60, no. 11, pp. 5214–5227, 2013.
 - [26] X. Chen, W. Wu, N. Gao, J. Liu, H. S.-H. Chung, and F. Blaabjerg, "Finite control set model predictive control for an LCL-filtered grid-tied inverter with full status estimations under unbalanced grid voltage," *Energies*, vol. 12, no. 14, p. 2691, 2019.
 - [27] A. Bendre, G. Venkataramanan, D. Rosene, and V. Srinivasan, "Modeling and design of a neutral-point voltage regulator for a three-level diode-clamped inverter using multiple-carrier modulation," *IEEE Transactions on Industrial Electronics*, vol. 53, no. 3, pp. 718–726, 2006.